Transients in shear thickening suspensions: When hydrodynamics matters

Shivakumar Athani [1] Bloen Metzger [2] Yoël Forterre [2] and Romain Mari [1]
[1] *Université Grenoble Alpes, CNRS, LIPhy*, 38000 Grenoble, France
[2] *Aix Marseille Université, CNRS, IUSTI*, 13453 Marseille, France

(Received 27 August 2024; accepted 4 March 2025; published 9 April 2025)

Using particle-based numerical simulations performed under pressure-imposed conditions, we investigate the transient dilation dynamics of a shear thickening suspension brought to shear jamming. We show that the stress levels, instead of diverging as predicted by steady-state flow rules, remain finite and are entirely determined by the coupling between the particle network dilation and the resulting Darcy backflow. System-spanning stress gradients along the dilation direction lead to cross-system stress differences scaling quadratically with the system size. Measured stress levels are quantitatively captured by a continuum model based on a Reynolds-like dilatancy law and the Wyart-Cates constitutive model. Beyond globally jammed suspensions, our results enable the modeling of inhomogeneous flows where shear jamming is local, e.g., under impact, which eludes usual shear thickening rheological laws.

DOI: 10.1103/PhysRevFluids.10.043301

I. INTRODUCTION

The abrupt shear thickening of dense non-Brownian suspensions is now understood as a frictional transition [1–9]. This transition occurs when suspended particles interact through a short-range repulsive force that prevents solid frictional contacts below a typical applied stress $P_{\mathrm{rep}} = f_{\mathrm{rep}}/a^2$, where f_{rep} is the amplitude of the repulsive force and a is the particle diameter [Fig. 1(a)]. Particles then virtually behave as if they were frictionless, yielding a jamming volume fraction ϕ_0 significantly larger than the critical packing fraction ϕ_1 of an assembly of frictional particles. Activating frictional contacts by increasing the applied stress above P_{rep} then leads to an increase in the suspension viscosity [2].

The most dramatic and interesting case is when the suspension volume fraction ϕ is prepared such that $\phi_1 < \phi < \phi_0$. The frictional transition then leads to shear jamming: the frictionless suspension can flow under small stresses [Fig. 1(b), orange circle], but jams above a critical stress, which implies that there is a maximum achievable shear rate, $\dot{\gamma}_{\max}(\phi)$ [Fig. 1(b), red circle] [10,11]. (We ignore here the possibility of achieving a higher shear rate by yielding or fracturing the jammed suspension, which would occur at stress values much larger than P_{rep}.) This situation is encountered during impact [12–15], but also in rheometric measurements in the thickened state, when intermittency arises from the emergence of transient localized jammed structures (see examples shown in Fig. 1(c) and Refs. [16–19]). Unfortunately, conventional constant-volume constitutive models based on the frictional transition [10,20–23] cannot predict the stress levels in this case: imposing a nonvanishing shear rate to a jammed system is simply impossible in their framework.

However, the above scenario only applies under strict volume-imposed conditions. In practice, jammed particulate systems can flow under any imposed shear rate, provided that the particle phase is allowed to dilate [24], for example, by deforming the capillary interface or by dilating into the surrounding unjammed suspension. In the presence of an interstitial fluid, dilation of the particle network induces a Darcy back flow, whose drag on the particles modifies the interparticle contact

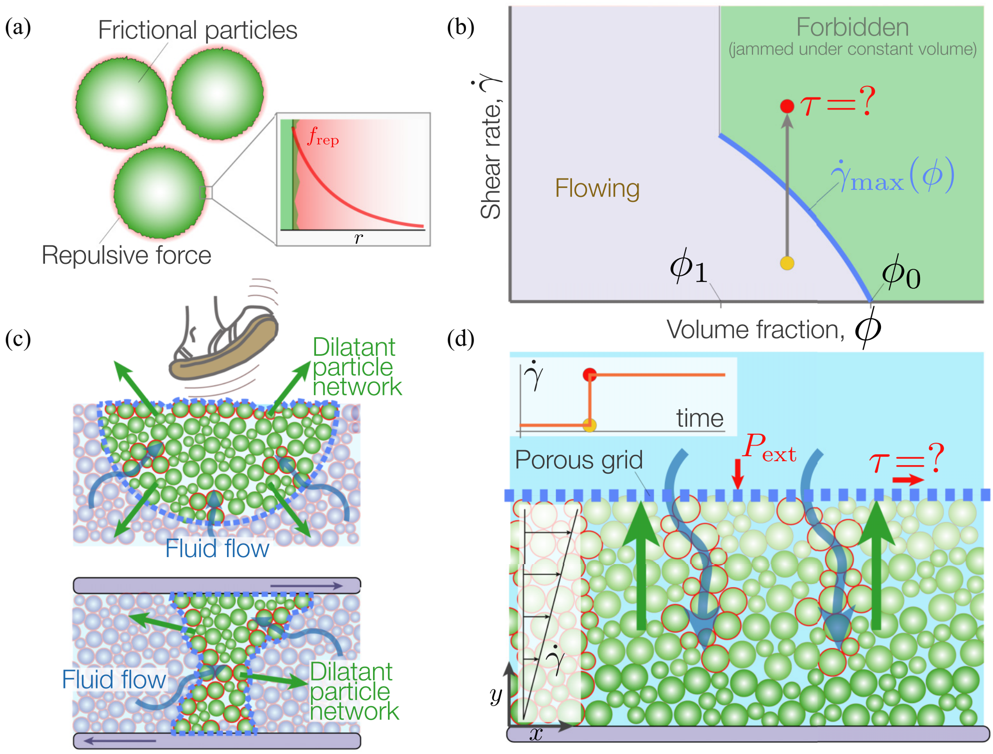

FIG. 1. Origin of stress during shear jamming of a shear thickening suspension. (a) Sketch of the frictional and repulsive particles. (b) Phase diagram [$\dot{\gamma} - \phi$] shear rate/volume fraction of a shear thickening suspension under constant volume conditions. There is no steady state above the $\dot{\gamma}_{\rm max}(\phi)$ line, which delineates the "forbidden" region (in green). (c) Examples of transient shear jamming during impacts and rheometric measurments. (d) Model configuration investigated: a shear thickening suspension under imposed external pressure $P_{\rm ext}$ is driven in the forbidden region by imposing a step increase in shear rate.

forces and thus the stress level. This pore-pressure feedback mechanism has been extensively studied in the context of soil mechanics or geophysics and has been shown to control the transient flow dynamics of fluid-saturated granular packing, prepared above or below their critical volume fraction [25–34]. Shear thickening suspensions are expected to be particularly prone to such feedback. First, they can be easily prepared above their jamming volume fraction by increasing the shear rate above $\dot{\gamma}_{\rm max}(\phi)$, and second, the small particle size and the large expected volume-fraction change during dilation should induce particularly strong Darcy pressure gradients. Previous studies have suggested these effects may play an important role in shear thickening suspensions [31,35–37]. The aim of the present study is to explore this role.

In this article, we clarify what controls the stress levels during transients in a dilating shear thickening suspension. In order to avoid the spatial and temporal complexities encountered during impact and/or rheometric measurements, while keeping the key physical ingredients, we use the simple shear configuration shown in Fig. 1(d). Discrete numerical simulations are performed under pressure-imposed conditions and the suspension, initially prepared such that $\phi_1 < \phi < \phi_0$ [Fig. 1(b), orange circle], is suddenly forced into the "forbidden" phase by imposing a step in the shear rate [Fig. 1(b), red circle]. We show that, during this transient, the resistance to flow of the suspension is entirely set by the coupling between the dilation dynamics and the Darcy backflow. A simple two-phase model, based on Wyart-Cates (WC) flow rules augmented with a Reynolds-like dilatancy law, quantitatively captures the stress level during dilation. The proposed model overcomes the dead end that pure constant-volume constitutive models face in situations where shear jamming occurs, and it highlights an overlooked role of hydrodynamics in setting stresses in nonhomogeneous flows of shear thickening suspensions.

II. METHODS

We simulate a monolayer of $N = 2000$ neutrally buoyant non-Brownian hard spheres immersed in a Newtonian fluid of viscosity η_0, placed between two rigid walls made of frozen particles separated by a mean distance H. We apply periodic boundary conditions along the horizontal (x) direction. The top wall is permeable to the fluid and subject to an externally applied normal stress $P_{\rm ext}$, but otherwise free to move vertically along the y direction. The bottom one is fixed and not permeable. A uniform shear $\dot\gamma$ is applied by prescribing a top wall horizontal velocity, $\dot\gamma H$. The background fluid velocity field $\boldsymbol{v}^\infty(y) = (\dot\gamma y, 0)$ acts on the particles via a Stokes drag, $6\pi\eta_0 a_i \boldsymbol{v}'_i$, where $\boldsymbol{v}'_i = \boldsymbol{v}_i - \boldsymbol{v}^\infty(y_i)$ is the nonaffine velocity of particle i, η_0 is the fluid viscosity, and a_i is the particle radius. This drag force first imposes a uniform particle shear rate across the layer, and second, it sets the Darcy backflow during dilation when particles move vertically (along the direction transverse to the flow) [34]. Particles are bidisperse, with a size ratio of 1.4 and a mean radius a, mixed in equal volume.

To simulate a shear thickening suspension, we use frictional particles of friction coefficient $\mu_{\rm p} = 0.5$ interacting via a zero-range repulsive force, $f_{\rm rep}$, using the critical load model [4]. We assume a Stokes flow and neglect inertial effects, so the equation of motion consists of the force balance,

$$\forall i: \quad 0 = \sum_j \boldsymbol{f}_{{\rm c},ij} - 6\pi\eta_0 a_i \boldsymbol{v}'_i + \sum_j \boldsymbol{f}_{{\rm lub},ij}, \tag{1}$$

and the torque balance, which takes a similar form [4]. Here $\boldsymbol{f}_{{\rm lub},ij}$ is the lubrication force that j exerts on i, and $\boldsymbol{f}_{{\rm c},ij}$ is the contact force. The contact force follows $|\boldsymbol{f}^{\rm t}_{{\rm c},ij}| \leqslant \mu_{\rm p} \max(|\boldsymbol{f}^{\rm n}_{{\rm c},ij}| - f_{\rm rep}, 0)$, with $\boldsymbol{f}^{\rm t}_{{\rm c},ij}$ and $\boldsymbol{f}^{\rm n}_{{\rm c},ij}$ being the tangential and normal parts. The critical load $f_{\rm rep} \equiv P_{\rm rep} a^2$ defines the thickening pressure scale [4]. The detailed implementation of contact and lubrication forces, as well as how the pressure is applied on the top wall, is given in the Appendix.

In the present configuration, the control parameters are the initial system size H/a, the viscous number $J_{\rm ext} \equiv \eta_0\dot\gamma/P_{\rm ext}$, and the reduced pressure $\hat P_{\rm ext} \equiv P_{\rm ext}/P_{\rm rep}$, whose value sets the particle's frictional state in the steady state [9,10,38]. The suspension friction coefficient is $\mu = \tau/P_{\rm ext}$, with τ being the mean shear stress, and the volume fraction (or solid fraction) is $\phi(t) \equiv N\pi a^2/\{l_x[H + \delta H(t)\}$, with l_x being the system horizontal length and $H + \delta H(t)$ the top wall position at time t.

III. RESULTS

A. Steady-state flow rules

The steady-state rheology of a shear thickening suspension under imposed particle pressure only depends on the viscous number $J_{\rm ext}$ and the reduced pressure $\hat P_{\rm ext}$ [2,10,38], and is characterized by two flow rules for the steady-state friction coefficient $\mu_{\rm st}(J_{\rm ext}, \hat P_{\rm ext})$ and the steady-state volume fraction $\phi_{\rm st}(J_{\rm ext}, \hat P_{\rm ext})$. Figure 2 shows the steady-state rheology of the suspension obtained from the DEM simulations performed under either low or high imposed external pressure (frictionless or frictional branches, respectively). The best fit of this data is used to set the Wyart and Cates flow rules used in the Darcy-Reynolds model.

In the limit of low $\hat P_{\rm ext} \ll 1$ (frictionless state), we obtain $\phi_{\rm st} = \phi_0 - k_0 J^{\beta_0}$, with $\phi_0 = 0.843$, $k_0 = 0.55$, and $\beta_0 = 0.5$, while at large $\hat P_{\rm ext} \gg 1$ (frictional state), $\phi_{\rm st} = \phi_1 - k_1 J^{\beta_1}$, with $\phi_1 = 0.809$, $k_1 = 0.68$, and $\beta_1 = 0.44$ [39]. Wyart-Cates flow rules [10] are then written as $\phi_{\rm st}(J, \hat P_{\rm p}) = \phi_{\rm J}(\hat P_{\rm p}) - K(\hat P_{\rm p}) J^{\beta(\hat P_{\rm p})}$, where $\phi_{\rm J}$, K, and β are functions interpolating between their frictionless and frictional limits. This interpolation is done using the fraction of frictional contacts f as

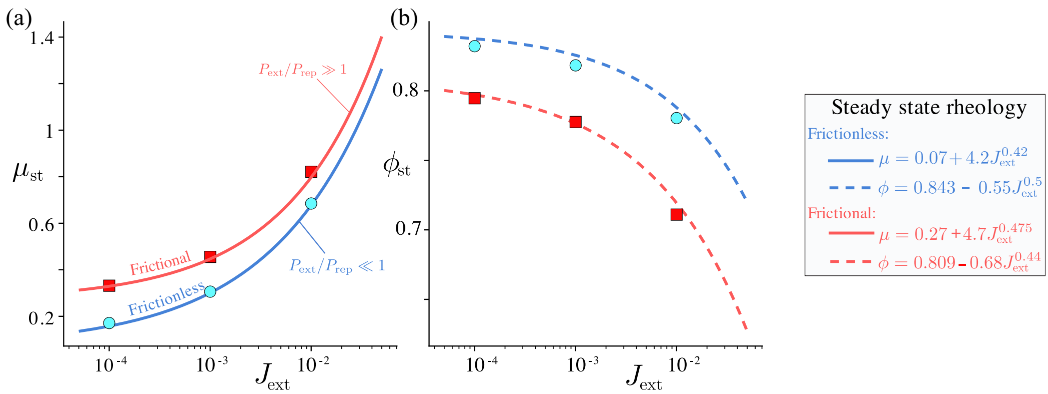

FIG. 2. Steady-state rheology of the shear thickening suspension. (a) Suspension friction coefficient μ and (b) volume fraction ϕ versus $J = \eta\dot{\gamma}/P_{\rm ext}$ obtained by setting $P_{\rm ext}/P_{\rm rep} \gg 1$ (frictional branch) or $P_{\rm ext}/P_{\rm rep} < 1$ (frictionless branch). Symbols: DEM simulations. Solid lines: Best fits to set the Wyart and Cates model.

an order parameter, which is defined as $f(\hat{P}_{\rm p}) = \exp(-A/\hat{P}_{\rm p})$. This yields $\phi_{\rm J}(\hat{P}_{\rm p}) = f\phi_1 + (1 - f)\phi_0$, $K(\hat{P}_{\rm p}) = fK_1 + (1 - f)K_0$, and $\beta(\hat{P}_{\rm p}) = f\beta_1 + (1 - f)\beta_0$ [21,23]. Only $A \approx 4.5$ is a shear-thickening-specific parameter and is adjusted to the steady rheology we measure.

B. Dilation dynamics

The suspension is initially prepared in a frictionless steady state by setting $\hat{P}_{\rm ext} \lesssim 1$ and choosing J_i small enough such that the initial ϕ lies between the frictionless and frictional jamming points, $\phi_1 < \phi = \phi_{\rm st}(J_i, \hat{P}_{\rm ext} \lesssim 1) < \phi_0$ [Fig. 1(d), orange circle]. At strain $\gamma = 0$, while keeping $\hat{P}_{\rm ext} \lesssim 1$ constant, we impose a sudden step increase in the shear rate, setting $J_f \equiv \eta_0\dot{\gamma}_f/P_{\rm ext} \gg J_i$, such that if the system was under constant volume, the suspension would instantly show infinite stresses [Fig. 1(d), red circle]. Instead, the pressure-imposed configuration used here allows the particle network to dilate, as shown by the evolution of the position of the top wall in Fig. 3(b). Although the external pressure $P_{\rm ext}$ is always kept constant and below $P_{\rm rep}$, the vertical dilation of the particle network induces a drag on the particles which increases the particles' stress $P_{\rm p}$ orders of magnitude above the onset stress to activate frictional contacts. During this transient, the particle pressure $P_{\rm p}$ within the layer is no longer set by the external pressure $P_{\rm ext}$ but results from the dilation dynamics. Figure 3 shows that dilation and the associated Darcy pressure gradient lead to a transient frictional transition occurring in most of the suspension layer [where $P_{\rm p}/P_{\rm rep} \gtrsim 10$, colored red in Fig. 3(b)] (see also our movie showning particlewise pressure during dilation [40]). At longer times, the suspension reaches a new steady state determined by the values of J_f and $\hat{P}_{\rm ext}$, and as the effects of dilation and Darcy backflow eventually vanish, the suspension returns to frictionless.

These DEM simulations allow us to estimate the particle pressure $P_{\rm p}^{\rm b}$ at the bottom of the layer (where it is largest), and the average shear stress τ that results from this step increase in shear rate. While WC flow rules under constant volume would predict an infinite shear stress and particle pressure [green curve in Fig. 3(c)], the dilation yields finite values with a maximum reached at the onset of dilation, for $\gamma = 0^+$ [red and purple curves in Fig. 3(c), respectively]. Interestingly, Fig. 4(a) shows that, for given values of J_i and J_f, the particle pressure $P_{\rm p}^{\rm b}(\gamma = 0^+)$ just after the step increase quadratically with the thickness of the layer H/a, such that $P_{\rm p}^{\rm b}/P_{\rm ext} \propto (H/a)^2$. We also find that, for the range of parameters investigated, dilation yields particle pressures $P_{\rm p}^{\rm b}$ reaching values $J_f = \eta\dot{\gamma}_f/P_{\rm ext}$ orders of magnitude larger than the imposed external pressure $P_{\rm ext}$.

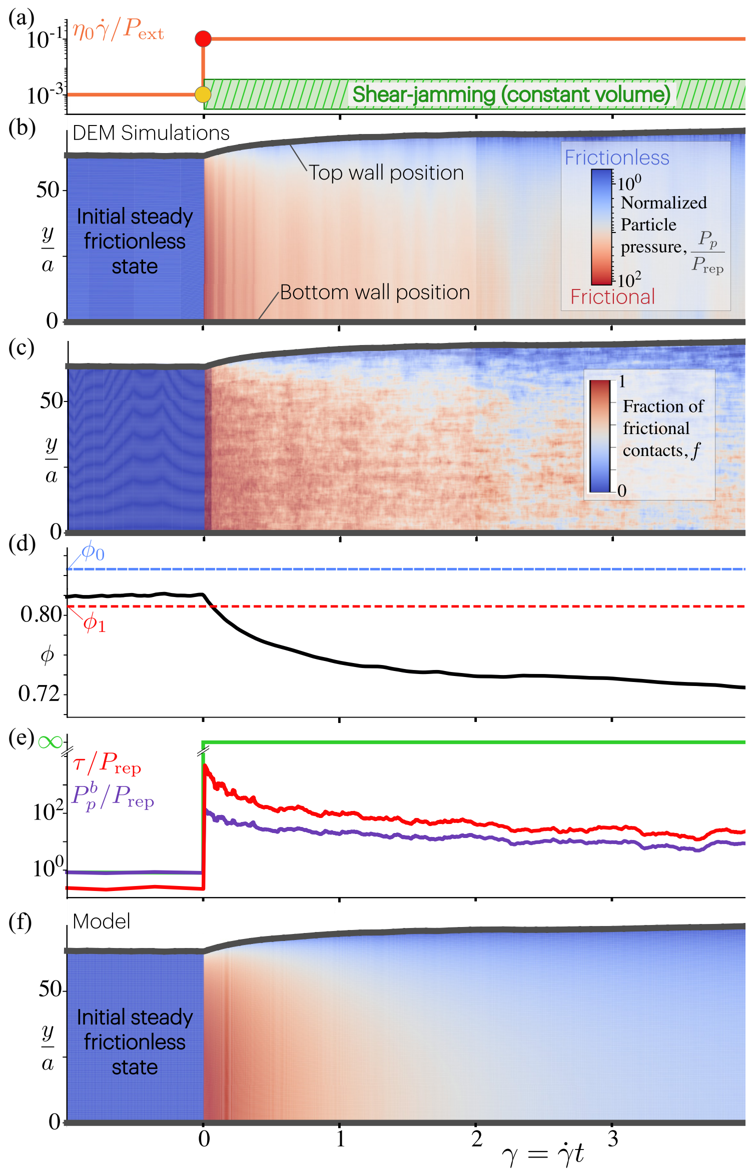

FIG. 3. Transient dilation of a shear jammed suspension yields finite stress. (a) Imposed step increase in shear rate keeping $\hat{P}_{\rm ext} = 0.75$ constant and choosing $J_i = 10^{-3}$ and $J_f = 10^{-1}$. Resulting evolution of (b) the top wall position and of the particle pressure $P_{\rm p}/P_{\rm rep}$ (color-coded) within the layer; (c) the fraction of frictional contacts, f (color-coded); (d) the mean volume fraction, ϕ; and (e) the average shear stress τ and the particle pressure at the bottom of the layer $P_{\rm p}^{\rm b}$. Green solid line: Flow rules under constant volume conditions. (d) Model [Eqs. (3) and (4)] solved for the same conditions to compare with panel (b) obtained from DEM simulations.

These trends can be rationalized as follows. When forced into the forbidden region, we assume that, in order to flow, the suspension dilates uniformly. Mass conservation then prescribes that $\partial_y v_y^{\rm p} = -(\partial_t \phi)/\phi \equiv \epsilon$, which defines the dilation rate ϵ, where $v_y^{\rm p}$ is the vertical component of the particle phase velocity due to dilation. The interphase drag force, resulting from the vertical motion of the grains, induces an additional pressure gradient on the particle phase $\partial_y P_{\rm p} \propto \eta_0 v_y^{\rm p}/a^2$.

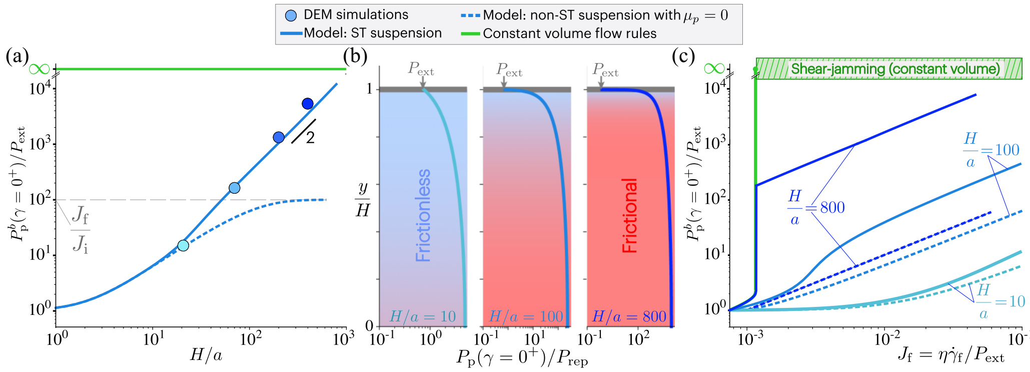

FIG. 4. Particle pressure: Finite-size and shear-rate effects. Particle pressure $P_{\rm p}^{\rm b}(\gamma = 0^+)/P_{\rm rep}$ at the bottom of the layer and just after the step versus layer thickness H/a ($\hat{P}_{\rm ext} = 0.2$, $J_i = 10^{-3}$, and $J_f = 10^{-1}$ constant). (b) Particle pressure profiles $P_{\rm p}(\gamma = 0^+)/P_{\rm rep}$ (color-coded to highlight the frictionless layer near the top wall) for different system sizes. (c) Particle pressure $P_{\rm p}^{\rm b}(\gamma = 0^+)/P_{\rm rep}$ versus final rescaled shear rate $J_f = \eta\dot{\gamma}_f/P_{\rm ext}$ ($\hat{P}_{\rm ext} = 0.75$ and $J_i = 10^{-3}$ constant).

Altogether, this gives $P_{\rm p}^{\rm b} - P_{\rm ext} \propto \eta_0\epsilon(H/a)^2$, which for large systems yields $P_{\rm p}^{\rm b} \propto \eta_0\epsilon(H/a)^2$, in agreement with Fig. 4(a).

C. Two-phase modeling

A more detailed two-phase model allows a refined understanding. Mass conservation on the solid phase is

$$\partial_t\phi + \partial_y\left(v_y^{\rm p}\phi\right) = 0. \tag{2}$$

Momentum conservation, in the approximation of the suspension balance model [41–44], balances the pressure gradient $\partial_y P_{\rm p}(y)$ with the local interphase drag, which is directly proportional to $v_y^{\rm p}$:

$$\partial_y P_{\rm p}(y) = -\frac{\eta_0}{a^2}\phi R(\phi) v_y^{\rm p}, \tag{3}$$

with $R(\phi)$ being the hydraulic resistance of the particle network, which is dimensionless in three dimensions. We use $R(\phi) = 6a$ to adapt to our two-dimensional simulations with a simple Stokes drag, with $P_{\rm p}$ now being a force per unit length. The model is closed with a Reynolds-like dilation law [45]:

$$\partial_t\phi + v_y^{\rm p}\partial_y\phi = -\frac{\dot{\gamma}}{\gamma_0}[\phi - \phi_{\rm st}(J, \hat{P}_{\rm p})], \tag{4}$$

where ϕ relaxes towards its steady-state value $\phi_{\rm st}(J, \hat{P}_{\rm p})$ (with $\hat{P}_{\rm p} = P_{\rm p}/P_{\rm rep}$) on a strain scale of γ_0 [46]. The steady rheology is given by the WC model, where for this shear thickening suspension, the steady-state solid fraction $\phi_{\rm st}(J, \hat{P}_{\rm p})$ depends on both J and $\hat{P}_{\rm p}$. Finally, boundary conditions are simply $v_y^{\rm p} = 0$ at the bottom wall and $P_{\rm p} = P_{\rm ext}$ at the top wall.

The evolution of the predicted particle pressure within the layer is shown in Fig. 3(d), which highlights the transient frictional transition induced by dilatancy, in good agreement with the DEM results obtained for the same conditions and shown in Fig. 3(b). Furthermore, Fig. 4(a) (blue solid line) shows that the model also captures the $(H/a)^2$ dependence of $P_{\rm p}^{\rm b}(\gamma = 0^+)$ for large system size. By contrast, for a frictionless (non-shear-thickening) suspension ($\mu_{\rm p} = 0$, blue dashed line), the solid fraction always remains below its jamming value ϕ_0. For large systems, the particle stress just after the step is then simply set by the steady-state flow rules, $P_{\rm p}^{\rm b}(\gamma = 0^+)/P_{\rm ext} = J_f/J_i$, and is independent of the dilation [39].

At this point, we highlight and discuss finite-size effects. Right after the step, the particle pressure profile $P_{\mathrm{p}}(\gamma = 0^+)$ instantaneously establishes across the layer [see Fig. 4(b)]. This is because $\partial_t \phi$ appears in both Eqs. (2) and (4), so that it can be eliminated to reveal that at any instant the pressure obeys a nonlinear second-order ordinary differential equation (ODE) [34]. Since the pressure profile must match the boundary condition $P_{\mathrm{p}}(y = H) = P_{\mathrm{ext}}$, there is always a region below the top wall which remains frictionless and unjammed (where $P_{\mathrm{p}}/P_{\mathrm{rep}} \lesssim 10$). Moreover, one also expects that $P_{\mathrm{p}}^{\mathrm{b}}(\gamma = 0^+) \to P_{\mathrm{ext}}$ when $H \to 0$. Altogether, this explains why, for small systems, the dependence of $P_{\mathrm{p}}^{\mathrm{b}}(\gamma = 0^+)$ on H is milder than H^2.

In Fig. 4(c), we further explore the influence of the magnitude of the step in the shear rate, keeping $\dot{\gamma}_i$ and P_{ext} constant, but varying systematically $\dot{\gamma}_f$ for different system sizes. As expected from Eq. (4), the particle pressure for large system sizes scales linearly with the imposed shear rate $\propto \dot{\gamma}_f$, whenever $\dot{\gamma}_f$ exceeds $\dot{\gamma}_{\max}(\phi)$, which is where the constant-volume rheology would predict that $P_{\mathrm{p}}^{\mathrm{b}}(\gamma = 0^+)$ diverges (green solid line). For smaller systems, the particle pressure is damped, again as a manifestation of the unjammed layer below the top wall.

IV. CONCLUSION AND DISCUSSION

To investigate the stress levels that develop when a shear thickening suspension is suddenly brought to shear jamming, we perform DEM simulations in a model pressure-imposed configuration where the suspension is allowed to dilate. We show that stresses do not diverge, as expected for strictly volume-imposed conditions. Instead, stresses remain finite and are determined entirely by the coupling between the Reynolds dilation and the Darcy backflow. In the large size limit, this Darcy-Reynolds coupling induces a particle pressure difference across the system that scales quadratically with the system size. We model and rationalize the above phenomenology with a two-phase migration law taking a Reynolds dilatancy form [39,45], the suspension balance model [41–44], and WC constitutive flow rules [10].

Our results show that a dilation, even minute, can be the source of very large transient stresses within the shear-jammed region. We anticipate that this mechanism could play an important role in determining the resistance of shear thickening suspensions to impulsive motion, such as during impact, as previously proposed [31]. Other mechanisms have been suggested, based on the inertia of the impactor [14], its ability to transmit stress to the boundaries [47–51], its elasticity [52,53], or its viscous drag at the boundaries [15]. Crucially these scenarii only give to the jammed region the role of a rigid stress transmitter, but there is also evidence of dilation-induced stresses in these systems [31]. Our simulations show that the particle pressure resulting from dilatancy reaches up to $10^3 P_{\mathrm{rep}}$ for system sizes $H/a \lesssim 400$. Extrapolating this value to actual flows on the centimeter scale, with particle sizes a in the micrometer range, we expect pressures $>10^6 P_{\mathrm{rep}}$. For a cornstarch suspension (with $P_{\mathrm{rep}} \approx 1$–$10$ Pa [54–56]), this yields about 10–100 bar, which is sufficient to transiently support the weight of a person. Interestingly, these dilation-induced stress values are also greater than the pressure required for the grains to pop out of the suspension-air interface, which is of the order of $10\Gamma/a$, where Γ is the water-air surface tension [57]. We therefore also expect dilation to be a major cause of free-surface fractures, as commonly observed for macroscopic flows of shear thickening suspensions [58].

More fundamentally, while the fluid plays no role in the frictional transition mechanism at the origin of the steady-state flow rules of shear thickening suspensions, we show here that the consideration of hydrodynamics is key to understanding their transient dynamics. Our results could therefore help to better understand the reported spatiotemporal fluctuations, which elude a steady-state description. Discontinuous shear thickening leads to flow instabilities, often associated with the formation of transient localized structures showing large stress gradients [16–20,35,56,59–64] and often appearing jammed or rigid [16–18]. Discontinuous shear thickening also correlates with surprisingly large volume fraction fluctuations [65,66]. Steady-state rheological models struggle to account for these fluctuations because of their extreme volume fraction sensitivity: a tiny local increase in volume fraction is quickly smeared out by an outward particle migration from the large increase in local pressure. We show with Eq. (4) that this stabilizing mechanism is not instantaneous, but instead takes a finite strain to act, thus weakening its effect. As it is well known that fluctuations and their dynamics have a key role close to critical points, explicit accounting of transient dilation effects on the dynamics of volume fraction fluctuations near jamming appears as a priority for future developments.

ACKNOWLEDGMENTS

This work was funded by ANR ScienceFriction (Grant No. ANR-18-CE30-0024). All the computations presented in this paper were performed using the GRICAD infrastructure, which is supported by Grenoble research communities.

APPENDIX: DISCRETE ELEMENT METHOD EQUATIONS OF MOTION

The granular suspension considered in this study is neutrally buoyant and we work in vanishing Stokes number and Reynolds number regimes; consequently, the equation of motion is just the force and torque balances on each particle. Forces include contact forces, lubrication forces, and, for the wall particles, external forces. For a pair of particles i and j with radii a_i and a_j at positions $\boldsymbol{r}_i$ and $\boldsymbol{r}_j$, we note $h_{ij} = 2(|\boldsymbol{r}_j - \boldsymbol{r}_i| - a_i - a_j)/(a_i + a_j)$ as the normalized gap between the particles and $\boldsymbol{n}_{ij} = (\boldsymbol{r}_j - \boldsymbol{r}_i)/|\boldsymbol{r}_j - \boldsymbol{r}_i|$ as the unit center-to-center vector.

The contact force on a particle i with radius a_i in contact with particle j (i.e., when $h_{ij} < 0$) can be decomposed in normal and tangential components as

$$\boldsymbol{f}_{\mathrm{c},ij} = \boldsymbol{f}^{\mathrm{n}}_{\mathrm{c},ij} + \boldsymbol{f}^{\mathrm{t}}_{\mathrm{c},ij}. \tag{A1}$$

Contacts fulfill a modified Coulomb's friction law $|\boldsymbol{f}^{\mathrm{t}}_{\mathrm{c},ij}| \leqslant \max[\mu_{\mathrm{p}}(|\boldsymbol{f}^{\mathrm{n}}_{\mathrm{c},ij}| - f_{\mathrm{rep}}), 0]$ with sliding friction coefficient μ_{p}. The introduction of f_{rep} ensures that particles are frictionless where interparticle forces are small, and frictional otherwise, ultimately leading to a shear thickening rheology. The force components $\boldsymbol{f}^{\mathrm{n}}_{\mathrm{c},ij}$ and $\boldsymbol{f}^{\mathrm{t}}_{\mathrm{c},ij}$ are modeled in a Cundall-Strack fashion [67,68], with normal and tangential couples of spring and dashpot:

$$\begin{aligned} \boldsymbol{f}^{\mathrm{n}}_{\mathrm{c},ij} &= k_{\mathrm{n}}\boldsymbol{\xi}^{\mathrm{n}}_{\mathrm{c},ij} + \gamma_{\mathrm{n}}\boldsymbol{v}^{\mathrm{n}}_{ij}, \\ \boldsymbol{f}^{\mathrm{t}}_{\mathrm{c},ij} &= k_{\mathrm{t}}\boldsymbol{\xi}^{\mathrm{t}}_{\mathrm{c},ij} + \gamma_{\mathrm{t}}\boldsymbol{v}^{\mathrm{t}}_{ij}, \end{aligned} \tag{A2}$$

where $\boldsymbol{\xi}^{\mathrm{n}}_{\mathrm{c},ij} = h_{ij}\boldsymbol{n}_{ij}$ is the normal spring stretch; $\boldsymbol{\xi}^{\mathrm{t}}_{\mathrm{c},ij}$ is the tangential spring stretch; $\boldsymbol{v}^{\mathrm{n}}_{ij} = (\boldsymbol{I} - \boldsymbol{n}_{ij}\boldsymbol{n}_{ij}) \cdot (\boldsymbol{v}_j - \boldsymbol{v}_i)$ is the normal velocity difference (with $\boldsymbol{I}$ being the identity matrix); $\boldsymbol{v}^{\mathrm{t}}_{ij} = \boldsymbol{v}_j - \boldsymbol{v}_i - \boldsymbol{v}^{(i,j)}_{\mathrm{n}} - (a_i\boldsymbol{\omega}_i + a_j\boldsymbol{\omega}_j) \times \boldsymbol{n}_{ij}$ is the tangential relative surface velocity, with $\boldsymbol{\omega}_i$ and $\boldsymbol{\omega}_j$ being the angular velocities of particles i and j; k_{n} and k_{t} are spring stiffnesses; and γ_{n} and γ_{t} are dashpot resistances. Finally, the contact torque on particle i from the contact with particle j is simply obtained as $\boldsymbol{t}_{\mathrm{c},ij} = a_i\boldsymbol{n}_{ij} \times \boldsymbol{f}_{\mathrm{c},ij}$.

Using the notation $\boldsymbol{F}_{\mathrm{c}} \equiv (\boldsymbol{f}_{\mathrm{c},1}, \ldots, \boldsymbol{f}_{\mathrm{c},N}, \boldsymbol{t}_{\mathrm{c},1}, \ldots, \boldsymbol{t}_{\mathrm{c},N})$ for the $3N$ vector of contact forces and torques on each particle, we have

$$\boldsymbol{F}_{\mathrm{c}} = -\boldsymbol{R}^{\mathrm{c}}_{\mathrm{FV}} \cdot \boldsymbol{V} + \boldsymbol{F}_{\mathrm{c,s}}, \tag{A3}$$

with $\boldsymbol{V} = (\boldsymbol{v}_1, \ldots, \boldsymbol{v}_N, \boldsymbol{\omega}_1, \ldots, \boldsymbol{\omega}_N)$ being the vector of velocities and angular velocities for each particle, $\boldsymbol{R}^{\mathrm{c}}_{\mathrm{FV}}$ the resistance matrix associated with dashpots, and $\boldsymbol{F}_{\mathrm{c,s}}$ the part of contact forces coming from springs. For hydrodynamic forces and torques $\boldsymbol{F}_{\mathrm{h}}$, we have [69]

$$\boldsymbol{F}_{\mathrm{h}} = -\boldsymbol{R}^{\mathrm{h}}_{\mathrm{FV}} \cdot \boldsymbol{V}' + \boldsymbol{R}_{\mathrm{FE}} : \boldsymbol{E}^{\infty}, \tag{A4}$$

with $\boldsymbol{V}' = \boldsymbol{V} - \boldsymbol{V}^{\infty}$ being the vector of nonaffine velocities and angular velocities for each particle, where $\boldsymbol{V}^{\infty}$ are the background velocities and angular velocities evaluated at the particles centers, and $\boldsymbol{E}^{\infty}$ is the symmetric part of the imposed velocity gradient $\nabla\boldsymbol{V}^{\infty}$. The resistance matrices $\boldsymbol{R}^{\mathrm{H}}_{\mathrm{FV}}$

and $\boldsymbol{R}_{\mathrm{FE}}$ contain Stokes drag and torque and regularized lubrication forces and torques at leading order in particle separation [4].

The equation of motion is thus

$$\boldsymbol{F}_{\mathrm{h}} + \boldsymbol{F}_{\mathrm{c}} + \boldsymbol{F}_{\mathrm{ext}} = 0\,, \tag{A5}$$

with $\boldsymbol{F}_{\mathrm{hxt}}$ being the external force/torque applied on each particle. Of course, $\boldsymbol{F}_{\mathrm{ext}}$ takes nonzero values only for the wall particles.

As the simulated system comprises frozen wall and bulk particles suspended in the fluid, we separate the total resistance matrix as

$$\boldsymbol{R}^{\mathrm{c}}_{\mathrm{FV}} + \boldsymbol{R}^{\mathrm{h}}_{\mathrm{FV}} \equiv \boldsymbol{R}_{\mathrm{FV}} = \begin{pmatrix} \boldsymbol{R}^{\mathrm{bb}}_{\mathrm{FV}} & \boldsymbol{R}^{\mathrm{bw}}_{\mathrm{FV}} \\ \boldsymbol{R}^{\mathrm{wb}}_{\mathrm{FV}} & \boldsymbol{R}^{\mathrm{ww}}_{\mathrm{FV}} \end{pmatrix}. \tag{A6}$$

The matrices $\boldsymbol{R}^{\mathrm{bb}}_{\mathrm{FV}}$, $\boldsymbol{R}^{\mathrm{bw}}_{\mathrm{FV}}$, $\boldsymbol{R}^{\mathrm{wb}}_{\mathrm{FV}}$, and $\boldsymbol{R}^{\mathrm{ww}}_{\mathrm{FV}}$ indicate the hydrodynamic resistance matrices including bulk-bulk, bulk-wall, wall-bulk, and wall-wall interactions, respectively. Similarly, the nonaffine velocities/angular velocities have also been separated into a bulk particle part $\boldsymbol{V}^{\mathrm{b}} - \boldsymbol{V}^{\infty}$ and a wall particle part $\boldsymbol{V}^{\mathrm{w}} - \boldsymbol{V}^{\infty}$,

$$\boldsymbol{V}' = \begin{pmatrix} \boldsymbol{V}'^{\mathrm{b}} \\ \boldsymbol{V}'^{\mathrm{w}} \end{pmatrix}. \tag{A7}$$

Note that the wall particles do not follow the affine flow $\boldsymbol{V}^{\infty}$ for three reasons. First, their velocity have a vertical component when the system dilates or contracts. Second, even the horizontal component of the velocity of a wall particle, say particle i, located at height y_i, does not match $\boldsymbol{U}^{\infty}(y_i)$ because the wall moves rigidly and is made of particles located at slightly different heights. Third, they are constrained to have vanishing angular velocity when the affine flow has a finite angular velocity.

We can then solve the equation of motion, Eq. (A5), for the bulk velocities to get

$$\boldsymbol{V}'^{\mathrm{b}} = \boldsymbol{R}^{\mathrm{bb}\;-1}_{\mathrm{FV}} \cdot \left[\boldsymbol{K}^{\mathrm{b}} - \boldsymbol{R}^{\mathrm{bw}}_{\mathrm{FV}} \cdot \boldsymbol{V}'^{\mathrm{w}}\right], \tag{A8}$$

with

$$\begin{pmatrix} \boldsymbol{K}^{\mathrm{b}} \\ \boldsymbol{K}^{\mathrm{w}} \end{pmatrix} = \boldsymbol{R}_{\mathrm{FE}} : \boldsymbol{E}^{\infty} + \boldsymbol{F}_{\mathrm{c,s}} - \boldsymbol{R}^{\mathrm{c}}_{\mathrm{FV}} \cdot \boldsymbol{V}^{\infty}. \tag{A9}$$

We further decompose the wall nonaffine velocity in horizontal and vertical components $\boldsymbol{V}'^{\mathrm{w}} = \boldsymbol{V}'^{\mathrm{w}}_{\mathrm{h}} + v_y \boldsymbol{Y}^{\mathrm{w}}$, where $\boldsymbol{Y}^{\mathrm{w}}$ is the vector corresponding to a unit nonaffine vertical velocity for particles belonging to the upper wall, and vanishing nonaffine velocity for particles of the lower wall. Thus, the scalar $v_y = \partial_t \delta H$ is the upper wall vertical speed.

Injecting Eq. (A8) in the wall part of Eq. (A5), and using Eq. (A7), we get

$$v_y \boldsymbol{B} \cdot \boldsymbol{Y}^{\mathrm{w}} = \boldsymbol{K}^{\mathrm{w}} - \boldsymbol{R}^{\mathrm{wb}}_{\mathrm{FV}} \cdot \boldsymbol{R}^{\mathrm{bb}\;-1}_{\mathrm{FV}} \cdot \boldsymbol{K}^{\mathrm{b}} - \boldsymbol{B} \cdot \boldsymbol{V}'^{\mathrm{w}}_{\mathrm{h}} + \boldsymbol{F}_{\mathrm{ext}}\,. \tag{A10}$$

Taking the dot product with $\boldsymbol{Y}^{\mathrm{w}}$, and using $\boldsymbol{Y}^{\mathrm{w}} \cdot \boldsymbol{F}_{\mathrm{ext}} = P_{\mathrm{ext}} l_x$, we get the vertical wall velocity

$$v_y = \frac{\boldsymbol{Y}^{\mathrm{w}} \cdot \left[\boldsymbol{K}^{\mathrm{w}} - \boldsymbol{R}^{\mathrm{wb}}_{\mathrm{FV}} \cdot \boldsymbol{R}^{\mathrm{bb}\;-1}_{\mathrm{FV}} \cdot \boldsymbol{K}^{\mathrm{b}} - \boldsymbol{B} \cdot \boldsymbol{V}'^{\mathrm{w}}_{\mathrm{h}}\right] + P_{\mathrm{ext}} l_x}{\boldsymbol{Y}^{\mathrm{w}} \cdot \boldsymbol{B} \cdot \boldsymbol{Y}^{\mathrm{w}}}\,. \tag{A11}$$

Imposing that the vertical component of the upper wall velocity is v_y ensures that the total force on the upper wall vanishes, and therefore that the applied pressure on the top wall is indeed P_{ext}.

---

[1] N. Fernandez, R. Mani, D. Rinaldi, D. Kadau, M. Mosquet, H. Lombois-Burger, J. Cayer-Barrioz, H. J. Herrmann, N. D. Spencer, and L. Isa, Microscopic mechanism for shear thickening of non-Brownian suspensions, Phys. Rev. Lett. **111**, 108301 (2013).

[2] R. Seto, R. Mari, J. F. Morris, and M. M. Denn, Discontinuous Shear Thickening of Frictional Hard-Sphere Suspensions, Phys. Rev. Lett. **111**, 218301 (2013).

[3] C. Heussinger, Shear thickening in granular suspensions: Interparticle friction and dynamically correlated clusters, Phys. Rev. E **88**, 050201(R) (2013).

[4] R. Mari, R. Seto, J. F. Morris, and M. M. Denn, Shear thickening, frictionless and frictional rheologies in non-Brownian suspensions, J. Rheol. **58**, 1693 (2014).

[5] N. Y. C. Lin, B. M. Guy, M. Hermes, C. Ness, J. Sun, W. C. K. Poon, and I. Cohen, Hydrodynamic and contact contributions to continuous shear thickening in colloidal suspensions, Phys. Rev. Lett. **115**, 228304 (2015).

[6] J. Comtet, G. Chatté, A. Niguès, L. Bocquet, A. Siria, and A. Colin, Pairwise frictional profile between particles determines discontinuous shear thickening transition in non-colloidal suspensions, Nat. Commun. **8**, 15633 (2017).

[7] C. Clavaud, A. Bérut, B. Metzger, and Y. Forterre, Revealing the frictional transition in shear-thickening suspensions, Proc. Natl. Acad. Sci. USA **114**, 5147 (2017).

[8] J. F. Morris, Lubricated-to-frictional shear thickening scenario in dense suspensions, Phys. Rev. Fluids **3**, 110508 (2018).

[9] B. Etcheverry, Y. Forterre, and B. Metzger, Capillary-Stress controlled rheometer reveals the dual rheology of shear-thickening suspensions, Phys. Rev. X **13**, 011024 (2023).

[10] M. Wyart and M. E. Cates, Discontinuous shear thickening without inertia in dense non-Brownian suspensions, Phys. Rev. Lett. **112**, 098302 (2014).

[11] R. Mari, R. Seto, J. F. Morris, and M. M. Denn, Nonmonotonic flow curves of shear thickening suspensions, Phys. Rev. E **91**, 052302 (2015).

[12] Y. S. Lee, E. D. Wetzel, and N. J. Wagner, The ballistic impact characteristics of Kevlar® woven fabrics impregnated with a colloidal shear thickening fluid, J. Mater. Sci. **38**, 2825 (2003).

[13] R. G. Egres, M. J. Decker, C. J. Halbach, Y. S. Lee, J. E. Kirkwood, K. M. Kirkwood, N. J. Wagner, and E. D. Wetzel, Stab resistance of shear thickening fluid (STF)-kevlar composites for body armor applications, in *Transformational Science and Technology for the Current and Future Force*, Selected Topics in Electronics and Systems (World Scientific, Singapore, 2006), Vol. 42, pp. 264–271.

[14] S. R. Waitukaitis and H. M. Jaeger, Impact-activated solidification of dense suspensions via dynamic jamming fronts, Nature (London) **487**, 205 (2012).

[15] M.-A. Brassard, N. Causley, N. Krizou, J. A. Dijksman, and A. H. Clark, Viscous-like forces control the impact response of shear-thickening dense suspensions, J. Fluid Mech. **923**, A38 (2021).

[16] G. Ovarlez, A. V. N. Le, W. J. Smit, A. Fall, R. Mari, G. Chatté, and A. Colin, Density waves in shear-thickening suspensions, Sci. Adv. **6**, eaay5589 (2020).

[17] V. Rathee, D. L. Blair, and J. S. Urbach, Localized transient jamming in discontinuous shear thickening, J. Rheol. **64**, 299 (2020).

[18] A. Gauthier, G. Ovarlez, and A. Colin, Shear thickening in presence of adhesive contact forces: The singularity of cornstarch, J. Colloid Interface Sci. **650**, 1105 (2023).

[19] E. Moghimi, J. S. Urbach, and D. L. Blair, Stress and Flow Inhomogeneity in Shear-Thickening Suspensions, J. Colloid Interface Sci. **678**, 218 (2024).

[20] H. Nakanishi, S.-I. Nagahiro, and N. Mitarai, Fluid dynamics of dilatant fluids, Phys. Rev. E **85**, 011401 (2012).

[21] A. Singh, R. Mari, M. M. Denn, and J. F. Morris, A constitutive model for simple shear of dense frictional suspensions, J. Rheol. **62**, 457 (2018).

[22] B. M. Guy, C. Ness, M. Hermes, L. J. Sawiak, J. Sun, and W. C. K. Poon, Testing the Wyart–Cates model for non-Brownian shear thickening using bidisperse suspensions, Soft Matter **16**, 229 (2020).

[23] R. Mari and R. Seto, Force transmission and the order parameter of shear thickening, Soft Matter **15**, 6650 (2019).

[24] O. Reynolds, LVII. On the dilatancy of media composed of rigid particles in contact. With experimental illustrations, London, Edinburgh, Dublin Philos. Mag. J. Sci. (1885).

[25] R. M. Iverson, M. E. Reid, N. R. Iverson, R. G. LaHusen, M. Logan, J. E. Mann, and D. L. Brien, Acute sensitivity of landslide rates to initial soil porosity, Science **290**, 513 (2000).

[26] M. Pailha, M. Nicolas, and O. Pouliquen, Initiation of underwater granular avalanches: Influence of the initial volume fraction, Phys. Fluids **20**, 111701 (2008).
[27] S. D. Kulkarni, B. Metzger, and J. F. Morris, Particle-pressure-induced self-filtration in concentrated suspensions, Phys. Rev. E **82**, 010402(R) (2010).
[28] L. Rondon, O. Pouliquen, and P. Aussillous, Granular collapse in a fluid: Role of the initial volume fraction, Phys. Fluids **23**, 073301 (2011).
[29] V. Topin, Y. Monerie, F. Perales, and F. Radjaï, Collapse dynamics and runout of dense granular materials in a fluid, Phys. Rev. Lett. **109**, 188001 (2012).
[30] B. Metzger and J. E. Butler, Clouds of particles in a periodic shear flow, Phys. Fluids **24**, 021703 (2012).
[31] J. J. Jerome, N. Vandenberghe, and Y. Forterre, Unifying impacts in granular matter from quicksand to cornstarch, Phys. Rev. Lett. **117**, 098003 (2016).
[32] A. Bougouin and L. Lacaze, Granular collapse in a fluid: Different flow regimes for an initially dense-packing, Phys. Rev. Fluids **3**, 064305 (2018).
[33] E. P. Montellà, J. Chauchat, B. Chareyre, C. Bonamy, and T. J. Hsu, A two-fluid model for immersed granular avalanches with dilatancy effects, J. Fluid Mech. **925**, A13 (2021).
[34] S. Athani, B. Metzger, Y. Forterre, and R. Mari, Transient flows and migration in granular suspensions: Key role of Reynolds-like dilatancy, J. Fluid Mech. **949**, A9 (2022).
[35] V. Rathee, J. Miller, D. L. Blair, and J. S. Urbach, Structure of propagating high-stress fronts in a shear-thickening suspension, Proc. Natl. Acad. Sci. USA **119**, e2203795119 (2022).
[36] A. Bougouin, B. Metzger, Y. Forterre, P. Boustingorry, and H. Lhuissier, A frictional soliton controls the resistance law of shear-thickening suspensions in pipes, Proc. Natl. Acad. Sci. USA **121**, e2321581121 (2024).
[37] L. Talon and D. Salin, On pressure-driven Poiseuille flow with non-monotonic rheology, Eur. Phys. J. E **47**, 52 (2024).
[38] J. Dong and M. Trulsson, Analog of discontinuous shear thickening flows under confining pressure, Phys. Rev. Fluids **2**, 081301(R) (2017).
[39] S. Athani, Y. Forterre, B. Metzger, and R. Mari, Transients in pressure-imposed shearing of dense granular suspensions, EPJ Web Conf. **249**, 09009 (2021).
[40] See Supplemental Material at http://link.aps.org/supplemental/10.1103/PhysRevFluids.10.043301 for movies showing particle-resolved pressure during dilation.
[41] P. R. Nott and J. F. Brady, Pressure-driven flow of suspensions: Simulation and theory, J. Fluid Mech. **275**, 157 (1994).
[42] J. F. Morris and J. F. Brady, Pressure-driven flow of a suspension: Buoyancy effects, Int. J. Multiphase Flow **24**, 105 (1998).
[43] J. F. Morris and F. Boulay, Curvilinear flows of noncolloidal suspensions: The role of normal stresses, J. Rheol. **43**, 1213 (1999).
[44] P. R. Nott, E. Guazzelli, and O. Pouliquen, The suspension balance model revisited, Phys. Fluids **23**, 043304 (2011).
[45] M. Pailha and O. Pouliquen, A two-phase flow description of the initiation of underwater granular avalanches, J. Fluid Mech. **633**, 115 (2009).
[46] S. Roux and F. Radjai, Texture-Dependent Rigid-Plastic Behavior, in *Physics of Dry Granular Media*, NATO ASI Series, edited by H. J. Herrmann, J.-P. Hovi, and S. Luding (Springer, Dordrecht, 1998), pp. 229-236.
[47] S. von Kann, J. H. Snoeijer, D. Lohse, and D. van der Meer, Nonmonotonic settling of a sphere in a cornstarch suspension, Phys. Rev. E **84**, 060401(R) (2011).
[48] I. R. Peters and H. M. Jaeger, Quasi-2D dynamic jamming in cornstarch suspensions: Visualization and force measurements, Soft Matter **10**, 6564 (2014).
[49] B. Allen, B. Sokol, S. Mukhopadhyay, R. Maharjan, and E. Brown, System-spanning dynamically jammed region in response to impact of cornstarch and water suspensions, Phys. Rev. E **97**, 052603 (2018).

[50] S. Mukhopadhyay, B. Allen, and E. Brown, Testing constitutive relations by running and walking on cornstarch and water suspensions, Phys. Rev. E **97**, 052604 (2018).

[51] E. Han, L. Zhao, N. Van Ha, S. T. Hsieh, D. B. Szyld, and H. M. Jaeger, Dynamic jamming of dense suspensions under tilted impact, Phys. Rev. Fluids **4**, 063304 (2019).

[52] Pradipto and H. Hayakawa, Impact-induced hardening in dense frictional suspensions, Phys. Rev. Fluids **6**, 033301 (2021).

[53] Pradipto and H. Hayakawa, Effective viscosity and elasticity in dense suspensions under impact: Toward a modeling of walking on suspensions, Phys. Rev. E **108**, 024604 (2023).

[54] A. Fall, N. Huang, F. Bertrand, G. Ovarlez, and D. Bonn, Shear thickening of cornstarch suspensions as a reentrant jamming transition, Phys. Rev. Lett. **100**, 018301 (2008).

[55] E. Brown and H. M. Jaeger, Dynamic jamming point for shear thickening suspensions, Phys. Rev. Lett. **103**, 086001 (2009).

[56] M. Hermes, B. M. Guy, W. C. K. Poon, G. Poy, M. E. Cates, and M. Wyart, Unsteady flow and particle migration in dense, non-Brownian suspensions, J. Rheol. **60**, 905 (2016).

[57] F. E. Hackett and J. S. Strettan, The capillary pull of an ideal soil, J. Agric. Sci. **18**, 671 (1928).

[58] E. Brown and H. M. Jaeger, Shear thickening in concentrated suspensions: Phenomenology, mechanisms and relations to jamming, Rep. Prog. Phys. **77**, 046602 (2014).

[59] S.-I. Nagahiro and H. Nakanishi, Negative pressure in shear thickening band of a dilatant fluid, Phys. Rev. E **94**, 062614 (2016).

[60] V. Rathee, D. L. Blair, and J. S. Urbach, Localized stress fluctuations drive shear thickening in dense suspensions, Proc. Natl. Acad. Sci. USA **114**, 8740 (2017).

[61] R. N. Chacko, R. Mari, M. E. Cates, and S. M. Fielding, Dynamic vorticity banding in discontinuously shear thickening suspensions, Phys. Rev. Lett. **121**, 108003 (2018).

[62] B. Saint-Michel, T. Gibaud, and S. Manneville, Uncovering instabilities in the spatiotemporal dynamics of a shear-thickening cornstarch suspension, Phys. Rev. X **8**, 031006 (2018).

[63] B. Darbois Texier, H. Lhuissier, Y. Forterre, and B. Metzger, Surface-wave instability without inertia in shear-thickening suspensions, Commun. Phys. **3**, 232 (2020).

[64] P. Angerman, B. Sandnes, R. Seto, and M. Ellero, Numerical simulations of spatiotemporal instabilities in discontinuous shear thickening fluids, arXiv:2408.08285.

[65] J. Bender and N. J. Wagner, Reversible shear thickening in monodisperse and bidisperse colloidal dispersions, J. Rheol. **40**, 899 (1996).

[66] X. Cheng, J. H. McCoy, J. N. Israelachvili, and I. Cohen, Imaging the microscopic structure of shear thinning and thickening colloidal suspensions, Science **333**, 1276 (2011).

[67] P. A. Cundall and O. D. L. Strack, A discrete numerical model for granular assemblies, Géotechnique **29**, 47 (1979).

[68] S. Luding, Cohesive, frictional powders: Contact models for tension, Granular Matter **10**, 235 (2008).

[69] D. J. Jeffrey, The calculation of the low Reynolds number resistance functions for two unequal spheres, Phys. Fluids A **4**, 16 (1992).